Autofocus for multispectral camera using focus symmetry

Hui-Liang Shen,[1,*] Zhi-Huan Zheng,[1] Wei Wang,[1] Xin Du,[1]
Si-Jie Shao,[2] and John H. Xin[2]

[1]Department of Information and Electronic Engineering, Zhejiang University, Hangzhou 310027, China

[2]Institute of Textiles and Clothing, The Hong Kong Polytechnic University, Hong Kong, China

*Corresponding author: shenhl@zju.edu.cn

A multispectral camera acquires spectral color images with high fidelity by splitting the light spectrum into more than three bands. Because of the shift of focal length with wavelength, the focus of each channel should be mechanically adjusted in order to obtain sharp images. Because progressive adjustment is quite time consuming, the clear focus must be determined by using a limited number of images. This paper exploits the symmetry of focus measure distribution and proposes a simple yet efficient autofocus method. The focus measures are computed using first-order image derivatives, and the focus curve is obtained by spline interpolation. The optimal focus position, which maximizes the symmetry of the focus measure distribution, is then computed according to distance metrics. The effectiveness of the proposed method is validated in the multispectral camera system, and it is also applicable to relevant imaging systems. © 2012 Optical Society of America

OCIS codes: 110.4234, 100.3020, 330.1710.

1. Introduction

A multispectral camera captures spectral color images by splitting the visible spectrum into more than three bands and records these bands as a series of monochrome images. When properly calibrated, the multispectral camera essential to practical applications where faithful color acquisition and reproduction are demanded. For example, multispectral imaging has been widely applied in scene simulation [1], digital archiving [2], skylight spectrum recovery [3], and spectral color measurement [4,5] as well.

A typical multispectral imaging system, as illustrated in Fig. 1, consists of a digital camera and a filter wheel equipped with a series of bandpass filters. The acquisition of a multispectral image is implemented by sequentially rotating these filters into the optical path of the camera and recording the cor-

responding images. However, the effective refractive indices of the filters and lens are wavelength dependent, and thus they change the focal lengths of the individual channels. This causes two problems, i.e., geometric distortion and optical blurring, in acquiring multichannel images. For the first problem, recent work [6] shows that images of different channels can be perfectly aligned by using camera calibration and an approximation of filter model. Recently, researchers attempted to solve the second problem by employing image deblurring algorithms, a fundamental issue in image processing [7,8]. In this work we are also interested in resolving the image blurring problem. But instead, we try to acquire clear multispectral images by employing an autofocus technique, based on focus adjustment with a step motor.

Autofocus is, actually, an essential function to digital cameras [9,10], and it has been applied in imaging systems such as iris recognition [11] and computer microscopes [12]. As exhaustive searching

Fig. 1. (Color online) Typical multispectral camera that consists of a digital camera and a filter wheel. Eight narrowband filters are installed in the filter wheel. Because of the wavelength-dependent refractive indices of the lens and filters, the appropriate lens position of each channel is adjusted by using a step motor.

L: Lens   Q: Optical center   D: Aperture diameter   F: Focal point
P: Object point   P': Image point   IP: Image plane   d: Lens movement
u: Object distance   v: Image distance

Fig. 2. Geometry of image formation and image blurring caused by the movement of the camera sensor or lens.

$$\frac{1}{f} = \frac{1}{u} + \frac{1}{v}, \qquad (1)$$

where u is the distance of the object point from the lens and v is the distance of its image from the lens.

However, when the sensor plane does not coincide with the image plane IP, the image point P' formed on the sensor will be a blurred circle. In Fig. 2, it is observed that when the sensor moves forward or backward with the same distance d, the blur radius is identical; i.e., $R_1 = R_2$. Note that, for the multispectral camera illustrated in Fig. 1, it is the lens position, not the sensor plane, that is adjusted using the step motor. Nevertheless, when the object distance u is much larger than the lens movement d, the change of the object distance is negligible; i.e., $u \pm d \approx u$. As a consequence, the movement of the lens is equivalent to the movement of the image sensor, as shown in Fig. 2.

To evaluate the sharpness of the acquired image, a variety of focus measures have been proposed in applications such as autofocus [15], depth from focus [16], and multifocus image fusion [17]. As an evaluation metric, focus measure is required to be unimodal, monotonic with respect to blur, and computationally effective. For robustness, the focus measures of image pixels are usually computed in a local window. In the literature, the most commonly employed focus measures are probably the Tenenbaum gradient (TEN) [18], gray-level variance (GLV), and sum of modified Laplacian (SML) [19]. As implied by their names, TEN is computed from image gradients, while GLV and SML are based on variance and the Laplacian, respectively. For more details, readers are referred to [16].

Autofocus has become an integral function to modern digital and video cameras, and a variety of autofocus algorithms have been developed in recent years. These algorithms include the mountain-climbing servo [20], fast hill-climbing search [13], modified fast climbing search with adaptive step size [21], and two-step search [10]. We note that most methods are based on the coarse-to-fine strategy, and the camera lens should unavoidably move back and forth. Chiu and Fuh [14] estimated the optimal

of optimal focus position is very time consuming, the existing work commonly adopts a coarse-to-fine strategy [9,10,13]. That is, a coarse step interval is first adopted to determine the approximate focus range, and then a fine step interval is used to locate the exact focus position. Chiu and Fuh [14] instead proposed a direct solution, in which the target focus position is computed by fitting the curve of the focus measures according to an empirical model.

In this paper, we propose a novel autofocus method for acquiring sharp multispectral images, based on the observation that the distribution of focus measure is symmetric. In the method, the optimal focus is directly estimated from coarse focus positions, and thus the commonly adopted fine-tuning step can be eliminated. The effectiveness of the proposed method is evaluated in a multispectral camera system, in terms of both lens position and focus measure accuracy.

The rest of this paper is organized as follows. Section 2 presents the background of the lens focus and multispectral camera, and Section 3 discusses the symmetry property of focus measure distribution. The symmetry-based autofocus method is proposed in Section 4. Section 5 presents the experimental results and discussion, and finally, Section 6 concludes the paper.

2. Background

In this section, we first review the principle of camera focus and autofocus techniques, and then we introduce the focus blurring problem in multispectral camera.

A. Camera Focus

Figure 2 shows a simple optical imaging system, in which the complicated lens and additional filters are regarded as a thin lens with equivalent focal length. Denote the focal length as f, the relation between the distances of object point P and its well-focused image point P' is given by the lens formula,

focus position directly, by employing an empirical model. However, there is no evidence that this empirical model is applicable to other imaging systems.

B. Multispectral Camera

Figure 1 shows the principle diagram of the multispectral camera system adopted in this work. The system consists of a monochrome digital camera, a photograph lens with 50 mm focal length, and a filter wheel. In total, eight narrow bandpass filters, with center wavelengths of 400, 440, ..., 680 nm, are equipped on the filter wheel. As in [7], the filter wheel is placed in front of the lens so that the critical optical path from lens to camera is not altered. Another configuration is to place the filter wheel between the camera and lens [6].

The filters used in this work consist of two reflecting stacks separated by even-order spacer layers, and they operate under the principle of the Fabry–Perot interferometer. One colored glass and one mirror-reflecting glass are added in each filter. Therefore, the effective refractive index of the filter is dependent on the wavelength film material and the refractive index of the colored glass. This results in the shifts of focal length for different imaging channels and causes the problem of chromatic aberration. Specifically, chromatic aberration is the phenomena that the lens cannot focus the light of different wavelengths onto exactly the same image plane.

In practice, an apochromatic lens, which combines three lenses with different chromatic dispersion, is always adopted to reduce chromatic aberration. Figure 3 shows the focal length shift of a typical apochromatic lens, in which the focal lengths at three wavelengths (red, green, and blue) are equal. However, as the multispectral camera utilizes more than three narrowband wavelengths, chromatic aberration cannot be eliminated by using an apochromatic lens.

To acquire sharp multispectral images, Vora *et al.* [1] manually adjusted the focuses of individual imaging channels. This is obviously not feasible for automated image capturing. Mansouri *et al.* modeled the point spread function (PSF) of the out-of-focus image as a circular disk and deblurred each channel image with a Wiener filter in the frequency domain [7].
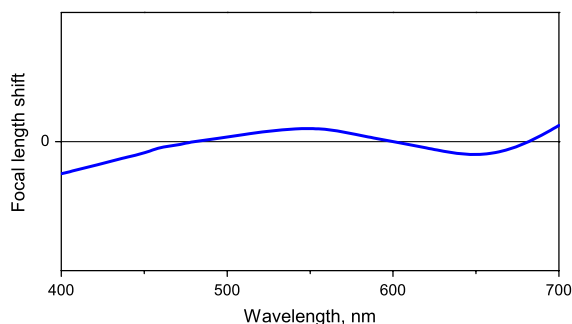
Fig. 3. (Color online) Focal length shift of a typical apochromatic lens with respect to the wavelength in the visible spectrum. As only three wavelengths are of equal focal length, the apochromatic lens is not suitable to a multispectral camera.

In this work, we adjust the focuses of individual channels automatically by using a step motor, as illustrated in Fig. 1. Compared with the work by Mansouri *et al.* [7], our method does not require PSF estimation and image deconvolution, and thus image artifacts will not occur. The problem to be solved is how to locate the optimal focus position with high efficiency.

3. Symmetry of Focus Measure Distribution

In this section, we theoretically shows that the PSF is solely determined by the lens movement distance, and this experimentally validates that the focus measure distribution is actually symmetrical.

A. Point Spread Function

As discussed above, the camera sensor deviating from the image plane will cause the image to be blurred. The focus blurred image $I(x,y)$, where x and y denote pixel position along the row and column directions, is formulated as the convolution of the ideal sharp image $I_{ideal}(x,y)$ and the PSF $h(x,y)$:

$$I(x,y) = I_{ideal}(x,y) * h(x,y), \qquad (2)$$

where $*$ denotes image convolution.

When acquiring planar samples at a relatively large object distance, the PSF can be considered to be spatial invariant. According to Eq. (2), the PSF can be computed by capturing two images, one blurred and one sharp, of an object. Without loss of generality, in this paper we adopt the common assumption that the PSF of focus blurring is Gaussian [22,23]:

$$h(x,y) = \frac{1}{2\pi\sigma^2} \exp\left(-\frac{x^2 + y^2}{2\sigma^2}\right). \qquad (3)$$

The variance σ is proportional to the radius R of the blur circle [24]:

$$\sigma = \beta R, \qquad (4)$$

where β is a constant depending on the optical system, and it can be determined by calibration if necessary.

As illustrated in Fig. 2, IP_1 and IP_2 are the camera detector positions located in front of and behind the image plane at a distance d, R_1 and R_2 are the corresponding radii of the two blur circles. Let D be the aperture diameter—based on the theorem of similar triangles, we have

$$R_1 = R_2 = \frac{Dd}{2v}. \qquad (5)$$

Equation (5) shows that when the lens moves forward or backward at a constant distance, the radii of the blurred circles are the same. Inserting Eq. (5) into Eq. (4), we get

$$\sigma = \frac{\beta D d}{2v} = \eta d, \tag{6}$$

where $\eta = \frac{\beta D}{2v}$.

Inserting Eq. (6) into Eq. (3) gives

$$h(x,y) = \frac{1}{2\pi\eta^2 d^2}\ \exp\left(\frac{-(x^2 + y^2)}{2\eta^2 d^2}\right). \tag{7}$$

This indicates that for a given optical geometry, the PSF, and consequently the blurred image, are completely determined by lens movement distance d, irrespective of the movement direction.

B. Distribution of Focus Measure

As we suppose the object to be imaged is planar in this work, the focus measure is computed for each channel on all pixels:

$$F = \frac{1}{K}\sum_x \sum_y |I_x(x,y)| + |I_y(x,y)|, \tag{8}$$

where I_x and I_y are image derivatives along the row and column directions, respectively, and K is a normalization factor. The basic calculation of the focus measure is similar to TEN [18] except that we use the absolute operator for computation efficiency.

The image derivatives are computed using Sobel operators. More specifically, we define the Sobel convolution kernels as

$$S_x = \begin{pmatrix} -1 & 0 & 1 \\ -2 & 0 & 2 \\ -1 & 0 & 1 \end{pmatrix}, \quad S_y = \begin{pmatrix} -1 & -2 & -1 \\ 0 & 0 & 0 \\ 1 & 2 & 1 \end{pmatrix}, \quad (9)$$

and then the image derivatives are computed as $I_x = S_x * I$ and $I_y = S_y * I$.

Note that, for multispectral images, the brightness of a channel may be quite different than other channels. For example, the multispectral image of a red sample has higher brightness in the long-wavelength channels than in the short-wavelength channels. To balance the magnitudes of focus measures for different channels, the normalization factor K is computed as

$$K = \sum_x \sum_y I(x,y). \tag{10}$$

Nevertheless, as the focus measures are computed for each channel independently, K can be omitted for computation efficiency.

Figure 4 shows the focus measure distributions of four channels out of eight for a planar sample. The lens position denotes the motor steps that move the lens from the origin position. The focus measures are computed from the channel images acquired at the corresponding lens positions, according to Eq. (8). It is observed that the distributions are all unimodal
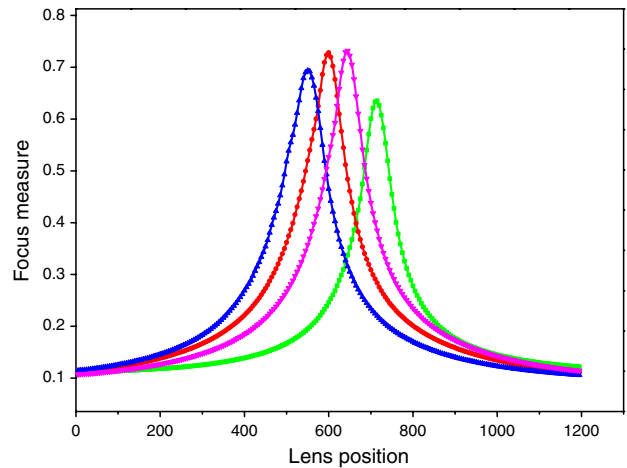
Fig. 4. (Color online) Distribution of focus measure at different channels. For clarity, only four out of eight distributions are displayed.

and approximately symmetrical with respect to the peaks. This is in accordance with the theoretical analysis of the PSF.

4. Autofocus

Autofocus estimates the optimal lens position that maximizes the symmetry of the focus measure distribution, preferably by acquiring only a limited number of images. Unlike most existing techniques [9,10], the proposed method does not employ the coarse-to-fine strategy. Compared with the work by Chiu and Fuh [14], the proposed method is nonparametric and does not require any empirical model.

Suppose that, for a certain channel, we have captured N images at a number of equidistant lens positions k_i, $1 \leq i \leq N$. The interval between adjacent lens positions is denoted as the number of motor steps to move the lens, and the focus measure $F(k_i)$ is computed according to Eq. (8). As illustrated in Fig. 5(a), the available focus points are relatively sparse. We simulate the focus measure distribution in the range $[k_1, k_N]$ using spline interpolation, and we obtain the interpolated focus curve $F(k)$, where $k \in [k_1, k_N]$. Note that the interpolated curve is similar to but different than the actual focus measure distributions illustrated in Fig. 4. For example, the actual distributions exhibit sharp peaks, while the interpolated curve does not, especially when the available lens positions are sparsely distributed. Nevertheless, as will be seen in the following, the interpolated curve is fundamental to our symmetry-based autofocus algorithm.

According to the unimodal property of the focus measure, the optimal lens position k_{opt} should be located between the positions corresponding to the maximum and second maximum focus measures. Letting k_T be the trial position, its optimal value should maximize the symmetry between the two half-curves at the left and right sides of k_T. We flip the left half-curve with respect to k_T, as illustrated
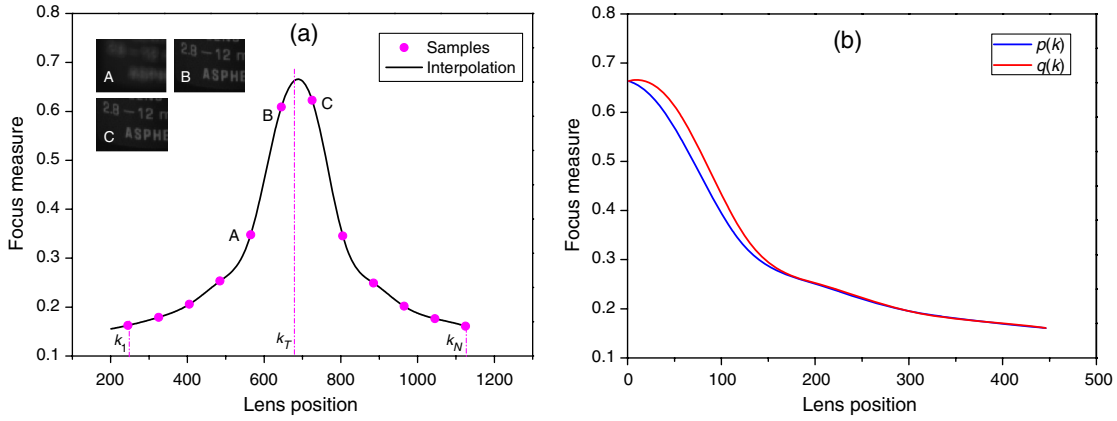
Fig. 5. (Color online) Illustration of symmetry computation. (a) Sampled lens position and its spline- interpolated curve. Three images corresponding to three lens positions (A, B, and C) are shown for visualization. (b) Focus measure distributions, $p(k)$ and $q(k)$, of the interpolated focus curve with respect to the trial lens position k_T in (a).

in Fig. 5, and we denote these two half-curves as distributions $p(k)$ and $q(k)$:

$$p(k) = F(k_T - k), \tag{11}$$

$$q(k) = F(k_T + k), \tag{12}$$

where $1 \le k \le \min(k_T - k_1, k_N - k_T)$. The two distributions, $p(k)$ and $q(k)$, should coincide in the case of ideal symmetry.

To evaluate the similarity between $p(k)$ and $q(k)$, several distance metrics can be employed. In this work, we investigate the norm-1 distance D_1, norm-2 (Euclidean) distance D_2, histogram intersection D_{HIST} [25], and Kullback-Leibler (KL) divergence D_{KL} [26].

The norm-1 distance is defined as the summed absolute focus measure differences of corresponding lens positions

$$D_1(p,q) = \sum_k |p(k) - q(k)|, \tag{13}$$

and the norm-2 distance is defined as

$$D_2(p,q) = \left(\sum_k \left(p(k) - q(k) \right)^2 \right)^{1/2}. \tag{14}$$

The histogram intersection [25] is widely used in image retrieval and object recognition, without considering the spatial relationship between pixels. In this work, by regarding the distributions $p(k)$ and $q(k)$ as histograms, we evaluate their similarity by

$$D_{HIST}(p,q) = 1 - \frac{\sum_k \min(p(k), q(k))}{\sum_k p(k)}. \tag{15}$$

Note that the more similar the two distributions are, the smaller D_{HIST} will be.

KL divergence is a measure of the difference between two probability distributions [26,27]. Although $p(k)$ and $q(k)$ are not true probability distributions, we can still compute the KL divergence as

$$D'_{KL}(p,q) = \sum_k p(k) \log \frac{p(k)}{q(k)}. \tag{16}$$

However, as $D'_{KL}(p,q) \ne D'_{KL}(q,p)$, the KL divergence is not a true distance metric. In this regard, we modify the KL divergence as

$$D_{KL}(p,q) = \sum_k p(k) \log \frac{p(k)}{q(k)} + \sum_k q(k) \log \frac{q(k)}{p(k)}$$
$$= \sum_k (p(k) - q(k)) \log \frac{p(k)}{q(k)}. \tag{17}$$

In this manner, D_{KL} is symmetrical and nonnegative, and it can be used as a distance metric to evaluate the similarity between $p(k)$ and $q(k)$.

5. Results and Discussion

The multispectral camera in this work is designed to acquire multispectral images of planar objects such as textile fabrics, artworks, and papers. The object distance u is above 1.2 m, much larger than the focal length of the lens ($f \approx 50$ mm). Because of the wavelength-dependent effective refractive indices of lens, the focal lengths vary for the eight imaging channels. As shown in Fig. 5(a), the adjustment of the lens position for each channel is in the range between 200 and 1150 steps, corresponding to several millimeters in lens movement d.

In the experiment, we acquired images with different step intervals and evaluated the effectiveness of the proposed autofocus method. For quantitative analysis, we computed the absolute position error between the actual best lens position k_{actual} and the estimated lens position k_{opt} as
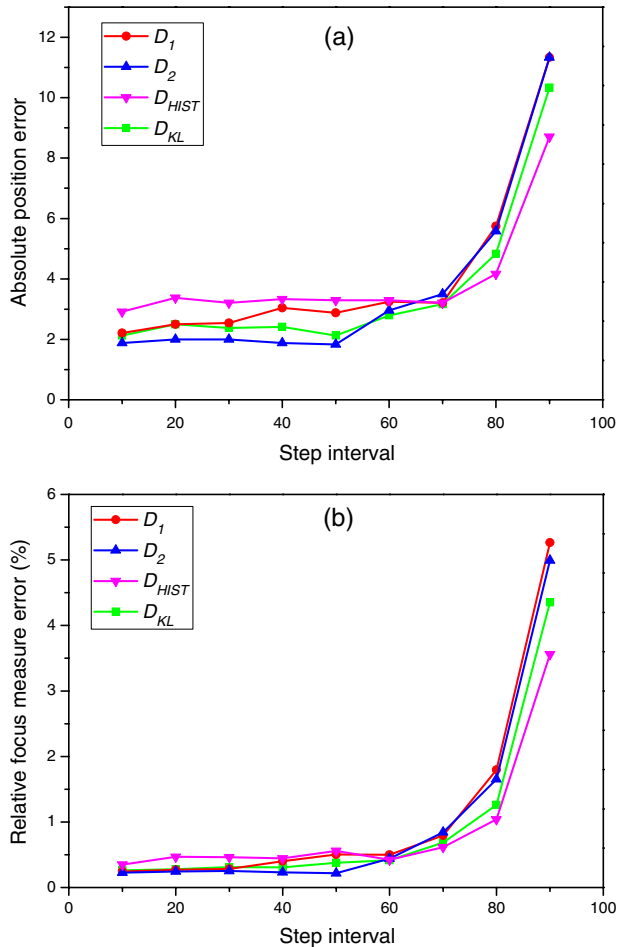
Fig. 6. (Color online) (a) Absolute lens position errors E_k and (b) relative focus measure errors E_F of various distance metrics, with respect to different step intervals.

$$E_k = |k_{\mathrm{actual}} - k_{\mathrm{opt}}|. \qquad (18)$$

In addition, the relative focus measure error between actual focus measure F_{actual} and the focus measure F_{opt} at the estimated position k_{opt} is computed as

$$E_F = \frac{|F_{\mathrm{actual}} - F_{\mathrm{opt}}|}{F_{\mathrm{actual}}} \times 100\%. \qquad (19)$$

We computed the averaged position errors and focus measure errors of the eight imaging channels from two textile fabrics and one paper (for images, see Fig. 7). Figure 6 shows the distributions of the errors with respect to different step intervals. It is observed that, for all distance metrics, the errors increases when the step interval becomes larger, because for large step intervals, the interpolation curve of the sparse points will be more different to the actual focus measure distribution. This will in turn affect the symmetry computation. From Fig. 6, the distance metric D_2 performs best when the step interval is less than 60, followed by D_{KL} and D_1, while D_{HIST} performs the worst. When the step interval is larger than 60, however, the metric D_{HIST} ranks first, followed by D_{KL}. The errors of D_1 and D_2 are relatively large.

Based on the above observation, we employed the D_2 metric and adopted a step interval 50. Under this interval, 20 images are acquired to compute the optimal focus position for each channel. Table 1 lists the absolute lens position errors E_k of the eight imaging channels for three planar samples. It is observed that all position errors are smaller than five steps, except for the 400 nm channel of sample Fabric2. The average position error is less than 2.5 steps. Table 2 shows the relative focus measure errors E_F, which are also very low. The average error magnitudes are less than 0.4%, which means that image sharpness acquired under the estimated lens position is nearly ideal.

The efficiency of the proposed method is compared with the traditional coarse-to-fine strategy. In the coarse-tuning stage, the motor moves with a step interval of 10 until the approximate focus range determined by the first and second maximum focus measures is found. In the fine-tuning stage, the motor moves with a step interval of 1 in that range to locate the target lens position. For the proposed method, the step interval stays at 50. Table 3 lists the average lens positions required for these two autofocus methods. Note that at each lens position the imaging procedure involves motor movement, image acquisition, and focus measure computation. Compared with this procedure, the computation time of the proposed optimal focus estimation is negligible. In this sense the efficiency improvement of the proposed method over the coarse-to-fine method reaches 65% $(= (57 - 20)/57)$, which will greatly benefit practical applications.

Figure 7 shows the three multispectral images, namely, Fabric1, Fabric2, and Paper, acquired with and without autofocus. The misalignment between channels, which was also caused by focal length shifts, was appropriately corrected. Then the reflectance spectrum of each pixel is reconstructed from camera responses based on the Wiener estimation [5]. In Fig. 7, the images were transformed to sRGB space [28] for visualization. It can be observed that due to the focal length shifts in these channels the

Table 1. Absolute Lens Position Errors E_k of Various Channels When Using the Norm-2 Distance Metric

Image	400 nm	440 nm	480 nm	520 nm	560 nm	600 nm	640 nm	680 nm	Average
Fabric1	0	0	2	1	4	0	0	0	0.88
Fabric2	8	2	0	3	4	2	1	0	2.50
Paper	1	1	4	3	5	1	0	2	2.13

Table 2. Relative Focus Measure Errors E_F of Various Channels When Using the Norm-2 Distance Metric

Image	400 nm	440 nm	480 nm	520 nm	560 nm	600 nm	640 nm	680 nm	Average
Fabric1	0	0	0.14	0.09	0.15	0	0	0	0.05
Fabric2	1.69	0.06	0	0.37	0.59	0.13	0.25	0	0.37
Paper	0.08	0.02	0.11	0.22	0.53	0.05	0	0.19	0.15

Table 3. Numbers of Lens Positions Required for the Coarse-to-Fine Method and the Proposed Autofocus Method

Coarse-to-Fine	Proposed	Improvement
57	20	65%

Table 4. Image Quality in the Case without (W/O) and with Autofocus, Evaluated in Terms of the PSNR and SSIM Metrics

Sample	PSNR		SSIM	
	W/O	With	W/O	With
Fabric1	34.0	43.7	0.841	0.987
Fabric2	35.0	42.3	0.838	0.972
Paper	38.6	45.5	0.945	0.978

images acquired without focus adjustment are obviously blurred. In comparison, the proposed autofocus technique considerably improves the sharpness of the flower patterns in the Fabric1 and Fabric2 samples. The improvement is more evident for the Paper sample, in which the characters are clearer after employing the autofocus technique.

The sharpness of the multispectral images illustrated in Fig. 7 is also evaluated with respect to the ideal sharp images in terms of the peak signal-to-noise ratio (PSNR) and structural similarity (SSIM) index [29]. Taking the structural information into account, SSIM is more consistent with human eye perception than the PSNR. Both metrics are computed between the ideal sharp image and the image under

evaluation. Table 4 shows that for all samples the image quality with autofocus is much better than that without autofocus in terms of both metrics. In the case with autofocus, the SSIM values of all samples are above 0.97. In the case without autofocus, the SSIM values of the Fabric1 and Fabric2 samples are about 0.84, while that of the Paper sample is much higher, reaching 0.945. This is because the Paper sample contains a large uniform area (see Fig. 7), and thus the image quality, on average, is less degraded by defocus blurring. The evaluation results using the PSNR metric are similar.

(a) Images without autofocus

(b) Images with autofocus

(c) Details of the highlighted regions
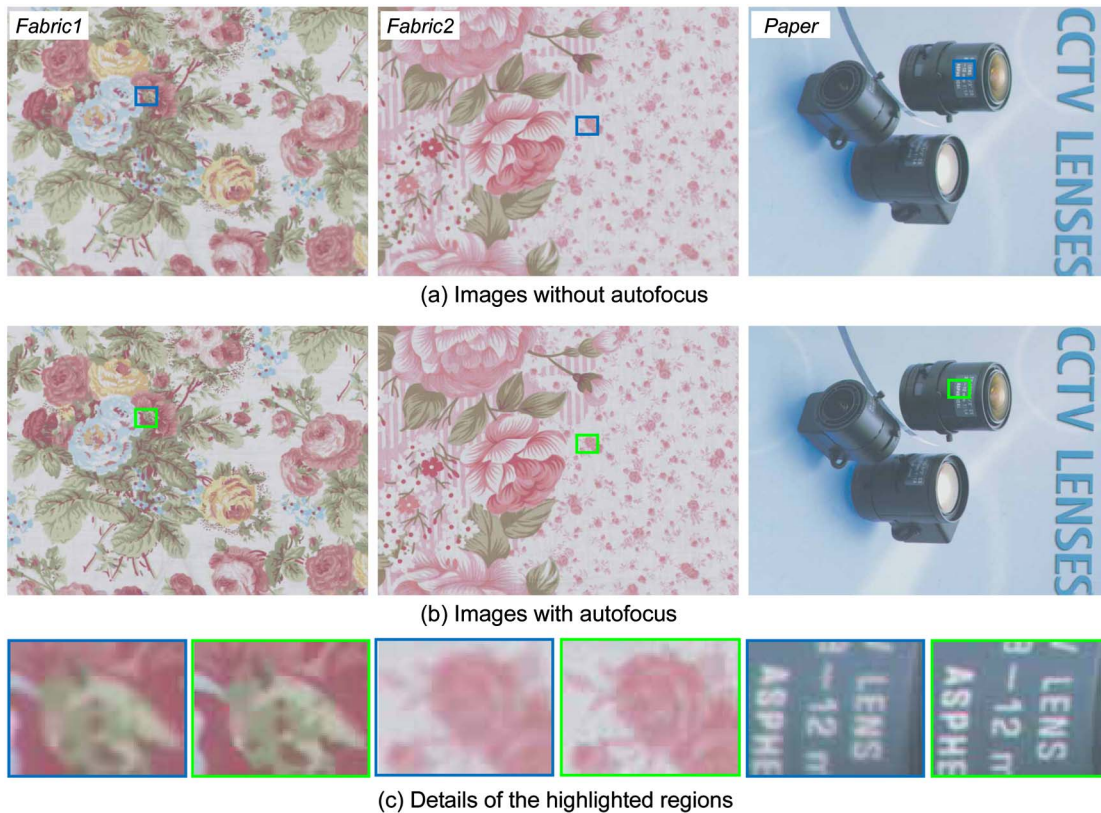
Fig. 7. (Color online) Acquired multispectral images without and with autofocus. The images are transformed to sRGB space for visualization.

6. Conclusions

This paper has proposed an autofocus method based on the symmetrical property of focus measure distribution. We verify this symmetry property through both theoretical analysis and practical results. To obtain sharp, clear multispectral images, for every channel a limited number of images are captured at individual lens positions and then the focus curve is obtained by spline interpolation. The optimal focus position, which maximizes the symmetry of focus measure distribution, is determined based on the appropriate distance metric. Experimental results validate that this proposed autofocus method performs quite well, and it can be used in a multispectral camera system or other relevant imaging applications.

References

1. P. L. Vora, J. E. Farrell, J. D. Tietz, and D. H. Brainard, "Image capture: simulation of sensor responses from hyperspectral images," IEEE Trans. Image Process. **10**, 307–316 (2001).
2. H. Haneishi, T. Hasegawa, A. Hosoi, Y. Yokoyama, N. Tsumura, and Y. Miyake, "System design for accurately estimating the spectral reflectance of art paintings," Appl. Opt. **39**, 6621–6632 (2000).
3. M. A. Lopez-Alvarez, J. Hernandez-Andres, E. M. Volero, and J. Romero, "Selecting algorithm, sensors, and linear bases for optimum spectral recovery of skylight," J. Opt. Soc. Am. A **24**, 942–956 (2007).
4. J. Gerhardt and J. Y. Hardeberg, "Spectral color reproduction minimizing spectral and perceptual color differences," Color Res. Appl. **33**, 494–504 (2008).
5. H. L. Shen, P. Q. Cai, S. J. Shao, and J. H. Xin, "Reflectance reconstruction for multispectral imaging by adaptive Wiener estimation," Opt. Express **15**, 15545–15554 (2007).
6. J. Brauers and T. Aach, "Geometric calibration of lens and filter distortions for multispectral filter-wheel cameras," IEEE Trans. Image Process. **20**, 496–505 (2011).
7. A. Mansouri, F. S. Marzani, J. Y. Hardeberg, and P. Gouton, "Optical calibration of a multispectral imaging system based on interference filters," Opt. Eng. **44**, 027004 (2005).
8. J. Brauers and T. Aach, "Longitudinal aberrations caused by optical filters and their compensation in multispectral imaging," in *IEEE International Conference on Image Processing (ICIP)* (IEEE, 2008), pp. 525–528.
9. C. M. Chen, C. M. Hong, and H. C. Chuang, "Efficient auto-focus algorithm utilizing discrete difference equation prediction model for digital still cameras," IEEE Trans. Consum. Electron. **52**, 1135–1143 (2006).
10. S. Y. Lee, Y. Kumar, J. M. Cho, S. W. Lee, and S. W. Kim, "Enhanced autofocus algorithm using robust focus measure and fuzzy reasoning," IEEE Trans. Circuits Syst. Video Technol. **18**, 1237–1246 (2008).
11. K. R. Park and J. Kim, "A real-time focusing algorithm for iris recognition camera," IEEE Trans. Syst. Man Cybern. **35**, 441–444 (2005).
12. Y. Sun, S. Duthaler, and B. J. Nelson, "Autofocusing in computer microscopy: selecting the optimal focus algorithm," Microsc. Res. Tech. **65**, 139–149 (2004).
13. K. S. Choi, J. S. Lee, and S. J. Ko, "New autofocusing technique using the frequency selective weighted median filter for video cameras," IEEE Trans. Consum. Electron. **45**, 820–827 (1999).
14. L. C. Chiu and C. S. Fuh, "An efficient auto focus method for digital still camera based on focus value curve prediction model," J. Inf. Sci. Eng. **26**, 1261–1272 (2010).
15. M. Subbarao and J. K. Tyan, "Selecting the optimal focus measure for autofocusing and depth-from-focus," IEEE Trans. Patt. Anal. Mach. Intell. **20**, 864–870 (1998).
16. S. O. Shim and T. S. Choi, "A novel iterative shape from focus algorithm based on combinatorial optimization," Patt. Recogn. **43**, 3338–3347 (2010).
17. W. Huang and Z. Jing, "Evaluation of focus measures in multi-focus image fusion," Patt. Recogn. Lett. **28**, 493–500 (2007).
18. J. M. Tenenbaum, "Accommodation in computer vision," Ph.D. thesis (Stanford University, 1970).
19. S. K. Nayar and Y. Nakagawa, "Shape from focus," IEEE Trans. Patt. Anal. Mach. Intell. **16**, 824–831 (1994).
20. K. Ooi, K. Izumi, M. Nozaki, and I. Takeda, "An advanced auto-focus system for video camera using quasi-condition reasoning," IEEE Trans. Consum. Electron. **36**, 526–530 (1990).
21. J. He, R. Zhou, and Z. Hong, "Modified fast climbing search auto-focus algorithm with adaptive step size searching technique for digital camera," IEEE Trans. Consum. Electron. **49**, 257–262 (2003).
22. A. P. Pentland, "A new sense for depth of field," IEEE Trans. Patt. Anal. Mach. Intell. **PAMI-9**, 523–531 (1987).
23. A. Aslantas, "A depth estimation algorithm with a single image," Opt. Express **15**, 5024–5029 (2007).
24. M. Subbarao, "Depth recovery from blurred edges," in *IEEE Computer Society Conference on Computer Vision and Pattern Recognition (CVPR)* (IEEE, 1988), pp. 498–503.
25. M. Swain and D. Ballard, "Color indexing," Int. J. Comput. Vis. **7**, 11–32 (1991).
26. S. Kullback and R. A. Leibler, "On information and sufficiency," Ann. Math. Stat. **22**, 79–86 (1951).
27. C. M. Bishop, *Pattern Recognition and Machine Learning* (Springer, 2006).
28. M. Stokes, M. Anderson, S. Chandrasekar, and R. Motta, "A standard default color space for the Internet: sRGB," Version 1.10, ICC (1996).
29. Z. Wang, A. C. Bovik, H. R. Sheikh, and E. P. Simoncelli, "Image quality assessment: from error visibility to structural similarity," IEEE Trans. Image Process. **13**, 600–612 (2004).